Asymmetric growth of strike-slip faults controlled by 3D fault structure: insights from the M_W 7.8 2023 Kahramanmaraş (Turkey) earthquake

Giovanni Camanni[1], Efstratios Delogkos[2], Stefano Tavani[3], Ester Piegari[4], Muhammed Kösen[5]

[1]Dipartimento di Scienze Chimiche e Geologiche, Università di Modena e Reggio Emilia, Modena, Italy

[2]Beicip-Franlab, 232 avenue Napoleon Bonaparte, 92500 Rueil-Malmaison, France

[3]Dipartimento di Scienze della Terra, Università di Firenze, Florence, Italy

[4]DiSTAR, Università degli Studi di Napoli "Federico II", Naples, Italy

[5]MK Prodüksiyon Tanıtım ve Film Hizmetleri, Merkez/Erzincan, Turkey

ABSTRACT

The reactivation of deep-seated, throughgoing strike-slip faults produces highly segmented fault zones at shallower levels, yet how displacement is partitioned among segments as the fault grows remains poorly constrained. We address this by examining a ~160 m long section of the East Anatolian Fault surface rupture of the M_W 7.8 2023 Kahramanmaraş strike-slip earthquake. The rupture offsets meter-spaced ridges and furrows in a ploughed field providing a unique opportunity for detailed displacement measurements, which were obtained from an orthophoto and a DEM built for this study. The surface rupture consists of ten primary segments separated by nine restraining stepovers and is associated with a 3D strain field dominated by ~3.5 m of left-lateral offset. Displacement patterns allow us to derive a new model for strike-slip fault growth in which

deformation is asymmetric and controlled by the 3D structure of the fault - specifically, by the position of the underlying fault relative to shallow fault segments. Initially, displacement is accommodated by contraction within restraining stepovers. With increasing displacement, fault segments located closer to the trace of the underlying fault consistently accumulate greater displacement. This asymmetry is facilitated by enhanced synthetic rotation within stepovers. With further displacement, the higher-displacement segment bounding a stepover becomes dominant, while the other one is bypassed and layer rotation ceases. These results not only improve fault growth models but could also inform seismic hazard models and impact industrial applications dealing with subsurface faulted reservoirs.

INTRODUCTION

Modelling and experimental studies, along with field observations of earthquake surface ruptures indicate that the reactivation of a deep-seated, throughgoing strike-slip fault typically leads to the development of a highly segmented fault zone at shallower levels (Cloos, 1928; Riedel, 1929; Tchalenko, 1970; Tchalenko and Ambraseys, 1970; Wilcox et al., 1973; Bartlett et al., 1981; Naylor et al., 1986; Swanson, 2006; Lin and Nishikawa, 2011; Dooley and Scheurs, 2012; Quigley et al., 2012; Ren et al., 2021; Yuan et al., 2022; Meng et al., 2024; Karabacak et al., 2023).

Most descriptions of these segmented faults agree on the following key characteristics about their geometry and growth. At the outset, the fault consists of multiple *en-echelon* segments known as Riedel (R) shears, forming a low angle to the strike of the underlying fault, and sharing its sense of shear (**Fig. 1A**). Serial cross-sectioning (Naylor et al., 1986) and CT scanning (Richard et al., 1995; Ueta et al., 2000; Yang et al., 2017) of analogue models suggest that R shears splay upward from the underlying fault in a helicoidal 3D geometry (**Fig. 1A**). Overlapping R shears

bound restraining zones, often referred to as restraining stepovers (**Fig. 1A**; Swanson, 2006; Pennacchioni and Mancktelow, 2013). With accumulating displacement, adjacent R shears link via P shears, also sharing the same sense of offset as the underlying fault but crossing it in the opposite direction of R shears (**Fig. 1B**), giving rise to a braided fault zone. Ultimately, displacement localizes onto a single fault that approximately coincides with the trace of the underlying fault.

Although this geometric evolution is well established, how displacement is partitioned among fault segments prior to localization, and the factors that control that partitioning, remain poorly constrained. This reflects the scarcity of natural and experimental examples where strike-slip faults intersect markers suitably oriented and spaced for detailed displacement measurements (see Peacock, 1991, and Pennacchioni and Mancktelow, 2013, for exceptions to this). Filling this knowledge gap is crucial, as it can provide fundamental insights into how faults grow from distributed to localized deformation.

We addrees this by examining a ~160 m long section of the surface rupture of the M_W7.8 February 6, 2023 Kahramanmaraş earthquake in south-east Turkey (Karabacak et al., 2023; Petersen et al., 2023; Reitman et al., 2023). The rupture is highly segmented and spectacularly offsets at high angle meter-spaced, sub-parallel ridges and furrows in a ploughed field (**Fig. 2A, B**), enabling exceptionally detailed displacement measurements.

THE FEBRUARY 6, 2023 KAHRAMANMARAŞ EARTHQUAKE(S)

On February 6, 2023, south-east Turkey and north Syria were struck by two major earthquakes (M_W7.8 and M_W7.6) occurring ~9 hours apart (Karabacak et al., 2023; Karabulut et al., 2023; Ozkan et al., 2023; Petersen et al., 2023; Reitman et al., 2023; Toker et al., 2023),

resulting in over 50000 fatalities. These events involved the reactivation of the East Anatolian left-lateral strike-slip fault system (EAFS), the transform plate boundary between the Anatolian and Arabian plates (Duman and Emre, 2013; **Fig. 2A**). This study focuses on the first, M_W7.8 earthquake which had its epicenter near the primary strand of the EAFS, and developed a surface rupture ~300 km long, with maximum left-lateral displacement of ~7 m (Karabacak et al., 2023; Liu et al., 2023; Meng et al., 2024; Ozkan et al., 2023; Reitman et al., 2023; Toker et al., 2023). The study area locates ~2km SE of the city of Türkoğlu (Turkey), ~20 km west of the epicenter (**Fig. 2A**). There the fault is ~NNE-SSW-striking and aftershock focal mechanisms indicate a component of co-seismic transtension, as opposed to north of Türkoğlu, where the fault strikes NE-SW strike and accommodated more purely strike-slip motion (Petersen et al., 2023).

DATA AND METHODS

The surface rupture was analyzed using a Digital Elevation Model (DEM) and an orthophoto built for this study from a ~25-second drone video acquired on February 11, 2023, five days after the earthquake. Together, these datasets allowed us to characterize the 3D (i.e., non-plane) strain field, comprising horizontal and vertical displacement components.

The aggregate horizontal component was quantified from the orthophoto as the sum of left-lateral separation of ridges and furrows in the ploughed field across fault segments (hereafter referred to as 'horizontal displacement') and synthetic (i.e., anticlockwise) rotation of ridges and furrows within stepovers occurring about a sub-vertical axis. The vertical component (hereafter referred to as 'vertical displacement') was measured from the DEM as the vertical separation relative to the undeformed ploughed field, which served as a 0-m elevation reference. The DEM

92 resolution (8.66 cm/pixel) provides a relative accuracy of ~ 2–3 cm, which we take as the
93 uncertainty of our horizontal and vertical displacement measurements.
94 Finally, a best-fit line through the midpoints between the boundaries of the surface rupture
95 was used as a proxy for the surface trace of the underlying fault. An extended description of data
96 and methods is provided in the Supplemental Material.
97
98 **GEOMETRY AND DISPLACEMENT PATTERNS OF THE SURFACE RUPTURE**
99 The surface rupture comprises ten primary fault segments (A–J) separated by nine
100 stepovers (S1–S9; **Fig. 2C**). Most stepovers occur as fault-bound lenses, forming a braided fault
101 configuration. The sigmoidal geometry of bounding segments (**Fig. 2C**) and their orientation
102 relative to the surface trace of the underlying fault (dashed gray line in **Fig. 2C**) suggest they
103 formed through linkage of R shears via P shears (**Fig. 1**). Intersections between adjacent segments
104 are classified as Y-zero and Y nodes (e.g., Manzocchi, 2002), based on whether displacement at
105 that location is null or not; isolated nodes are termed tip points. The positioning of Y-zero nodes
106 and tip points consistently indicates *en-echelon*, right-stepping geometry. Given the left-lateral
107 sense of movement of the fault, all stepovers are restraining.
108 The horizontal component of displacement yields an average aggregate value of ~3.5 m
109 (**Fig. 2D**), consistent with nearby field (3.3–3.8 m; Karabacak et al., 2023) and seismological
110 (Toker et al., 2023) estimates. Two stepover groups were recognized based on the distribution of
111 horizontal displacement. Stepovers S1, S4, S7, and S9 are bound by segments that exhibit inversely
112 increasing displacements and null-displacement points (Y-zero nodes or tips) on opposite stepover
113 sides (**Fig. 2C**). For example, at S1, segment A increases in displacement SW-ward from its tip
114 point to ~3.5 m beyond the stepover, whereas segment B shows a complementary NE-ward

115 increase (**Fig. 2B, C**). Displacement gradients are asymmetric - one segment shows a steeper
116 gradient and larger horizontal displacement at the stepover center (e.g., displacement gradient, and
117 amount of horizontal displacement at the center of S1, are larger for A than for B). Synthetic
118 rotation also increases toward the tip of the higher-gradient segment, as at S9, where segment I has
119 a larger displacement gradient than segment J, and synthetic rotation reaches its maximum
120 magnitude value of ~1 towards the tip of segment I (**Fig. 2D**). Conversely, stepovers S2, S3, S5,
121 S6, and S8 are bound by one segment ending in a Y-zero node/tip point and another ending in a Y
122 node on opposite sides (**Fig. 2C**). For instance, at S8, segment H increases in displacement
123 southwestward from its Y-zero node, while segment I increases northeastward but retains ~1.7 m
124 displacement at its Y node (**Fig. 2C**). In these cases, maximum values of horizontal displacement
125 and rotation occur near the Y node side of the stepover (**Fig. 2D**).

126 In all stepovers, the bounding segment with the larger horizontal displacement locates
127 closer to the surface trace of the underlying fault (**Fig. 2C**). This relationship is shown in **Fig. 3**,
128 where segment distance from the trace of the underlying fault (D left and D right) and horizontal
129 displacement (HD left and HD right) are plotted for each stepover; all measures were taken at the
130 center of each stepover. In every case, smaller distance to the underlying fault corresponds to larger
131 horizontal displacement, and vice versa (**Fig. 3**).

132 Vertical displacement is highly subordinate to the aggregate horizontal displacement
133 (maximum value of ~20 cm is ~5% of the maximum aggregate horizontal displacement, ~4 m;
134 **Fig. 2E**) and is localized and restricted to uplift within restraining stepovers, the larger of which
135 (~20 cm) occurs within stepover S1 (**Fig. 2E**).

136 A final deformation component consists of open fissures developed along the length of
137 some fault segments due to their 'opening' in a direction nearly perpendicular to the segment

strike; examples occur along segment I, segment H to the SSW of stepover S8, and segment F to the SSW of stepover S6 (**Fig. 2B**).

DISCUSSION AND IMPLICATIONS

Building on the displacement patterns described above, we further develop the strike-slip fault growth model in **Fig. 1** by incorporating both horizontal and vertical components of displacement. Open fissures are not included, as we interpret them as local features that either accommodate the extensional component of the transtensional co-seismic strain affecting this portion of the EAFS (Petersen et al., 2023) or form due to reduced confinement at the free surface. In both cases, they can be considered deformation components not intrinsic to strike-slip fault growth. Although the linkage between surface segments and the underlying fault cannot be directly imaged here, by analogy with previous studies (e.g., Naylor et al., 1986), we interpret the segments to connect downward to the deeper fault (**Fig. 4**); even if they were physically disconnected, their systematic *en-echelon* arrangement and consistent sense of stepping strongly suggest structural control by the underlying fault; thus, the interpretation presented below would remain valid.

In our interpretation, the fault initially comprises R shears that, where overlapping, bound restraining stepovers (**Fig. 1A**). As displacement accumulates, we identify three successive evolutionary stages (**Fig. 4**). At first, displacement gradients toward the tip points of R shears are accommodated through contraction confined within restraining stepovers (**Fig. 4A**). With increased displacement, adjacent R shears link through the development of P shears at Y-zero nodes. The resulting sigmoidal segment located closer to the trace of the underlying fault begins to accrue more displacement than the other, developing a larger displacement gradient towards its Y-zero node (**Fig. 4B**). This produces an asymmetric displacement deficit within the stepover,

greatest toward the tip of the higher-displacement segment (**Fig. 4B**) and is compensated by synthetic layer rotation. For ease of description, contraction and layer rotation are here described as successive processes although they may also operate simultaneously. With further displacement, the segment with larger displacement gradient becomes dominant, and its Y-zero node evolves into a Y node. Beyond this point, rotation stops and displacement localizes on the higher-displacement segment, while the adjacent segment bypassed (i.e., 'dead'; **Fig. 4C**).

This new model demonstrates that strike-slip faults grow asymmetrically and that this asymmetry is fundamentally controlled by the 3D structure of the fault – i.e., the position of the underlying throughgoing fault relative to shallow fault segments. Beyond enhancing fault growth models, these results also improve understanding of surface rupture development in active regions. Surface ruptures represent major geohazards and are widely designated as 'capable faults' in regulatory frameworks (e.g., IAEA, 2010). The ability to anticipate where the segment with the largest displacement is most likely to develop at the surface (given knowledge of the position of the pre-existing underlying fault) can help refine seismic-hazard assessment models (e.g., Piccardi et al., 2017; Bonini et al., 2025). These results may also have implications on the management of subsurface faulted reservoirs (e.g., Sun et al., 2023). In particular, given knowledge of the 3D geometry of a strike-slip fault (e.g., from 3D seismic reflection data), these results can help predict how displacement is distributed among fault segments even in the absence of clear displacement markers. This, in turn, can improve the identification of zones where higher strain and block rotation are expected, which may correspond to regions of enhanced fracturing and damage that could facilitate fluid flow.

ACKNOWLEDGMENTS

Glenn Biasi and two anonymous reviewers are kindly acknowledged for their comments. We are especially grateful to Bob Holdsworth for his guidance and the many insightful suggestions. Tracy Rushmer is thanked for her support and editorial handling of the manuscript. Finally, G.C. and E.D. would like to dedicate this manuscript to Conrad Childs, in recognition of his distinguished career and recent retirement.

FIGURE CAPTIONS

Figure 1. Structure and evolution of strike-slip faults with displacement accrual. **A**: segmented stage with *en-echelon* Riedel (R) shears (after Naylor et al., 1986); **B**: linkage stage where adjacent R shears connect via P shears. Segments splay upward from a throughgoing fault in a helicoidal 3D geometry.

Figure 2. Section of the East Anatolian Fault surface rupture produced by the M_W 7.8 2023 Kahramanmaraş earthquake, near Türkoğlu (Turkey). The surface rupture offsets at high angle, meter-spaced ridges and furrows in a ploughed field. **A**: Simplified tectonic map (modified after Liu et al., 2023) of the February 6, 2023 Kahramanmaraş earthquake doublet - surface ruptures (red lines) are from Reitman et al., 2023, and focal mechanisms from United States Geological Survey, Earthquakes (USGS, 2023; https://usgs.gov/programs/earthquake-hazards/earthquakes). Inset rectangle (Google Maps image) locates the study area in a broader portion of the surface rupture; **B**: Orthophoto of the surface rupture; **C**: map of the rupture. Colored bands correspond to single or grouped ridges and furrows correlated across the surface rupture. Names of segments (A to J) are on the left side of the segment they refer to. S1 to S9 are stepover names. The dashed grey

line along the surface rupture strike corresponds to the calculated surface trace of the underlying fault (see also Supplemental Material); **D**: profiles of horizontal displacement (left-lateral displacement, and synthetic rotation expressed as the displacement-equivalent produced by ridges/furrows anticlockwise rotation within stepovers), sub-horizontal grey dashed lines across **C** and **D** indicate the center of each stepover. All markers used for measurements and the data are provided in **Fig. S4**; **E**: DEM of the surface rupture.

Figure 3. Plot showing, for each stepover (S1 to S9): i) the distance of its left (D left) and right (D right) bounding segments from the surface trace of the underlying fault (see **Fig. 2C**); ii) the horizontal displacement on the left (HD left) and the right (HD right) segments. Measures of distance and displacement were taken at the center of each stepover (see **Fig. 2**). In all cases, a shorter distance of a segment from the trace coincides with its larger horizontal displacement, and vice versa.

Figure 4. Asymmetric strike-slip fault growth model illustrated for the stepover of **Fig. 1**. For each stage, a schematic profile of horizontal displacement is provide. **A**: contraction within the stepover; **B**: linkage of R shear via P shears; enhanced displacement on the segment nearer the trace of the underlying fault causes an asymmetric displacement deficit within the stepover compensated by synthetic layer rotation; **C**: the higher-displacement segment becomes dominant while the other is bypassed and rotation ceases.

REFERENCES CITED

Angelier, J., Bergerat, F., Bellou, M., Homberg, C., 2004, Co-seismic strike–slip fault displacement determined from push-up structures: the Selsund Fault case, South Iceland: Journal of Structural Geology, v. 26, p. 709-724, https://doi.org/10.1016/j.jsg.2003.07.006

Bartlett, W.,L., Friedman, M., Logan, J. M., 1981, Experimental folding and faulting of rocks under confining pressure Part IX. Wrench faults in limestone layers: Tectonophysics, v. 79 (3-4), p. 255-277, https://doi.org/10.1016/0040-1951(81)90116-5

Bonini, S., Asti, R., Viola, G., Tartaglia, G., Rodani, S., Benedetti, G., Comedini, M., Vignaroli, G., 2025, The impact of active and capable faults structural complexity on seismic hazard assessment for the design of linear infrastructures: Natural Hazards and Earth System Sciences, v. 25, p. 2981-2998, https://doi.org/10.5194/nhess-25-2981-2025

Cloos, H., 1928. Experimente zur inneren Tektonik: Centralblatt für Mineralogie, v. 12, p. 609-621

Dooley, T. P., Schreurs, G., 2012, Analogue modelling of intraplate strike-slip tectonics: A review and new experimental results: Tectonophysics, v. 574–575, p. 1-71, https://doi.org/10.1016/j.tecto.2012.05.030.

Duman, T., Y., Emre, Ö., 2013, The East Anatolian Fault: geometry, segmentation and jog characteristics: Geological Society, London, Special Publications, v. 372, p. 495-529, https://doi.org/10.1144/SP372.14

International Atomic Energy Agency: Seismic Hazards in Site Evaluation for Nuclear Installations, Specific Safety Guide No. SSG9, Vienna, ISBN 978–92–0–102910–2, 2010.

Karabacak, V., Özkaymak, Ç., Sözbilir, H., Tatar, O., Aktuğ, B., Cevdet Özdağ, Ö., Çakir, R., Aksoy, E., Koçbulut, F., Softa, M., Akgün, E., Demir, A., Arslan, G., 2023, The 2023 Pazarcık (Kahramanmaraş, Türkiye) earthquake (Mw 7.7): implications for surface rupture dynamics along the East Anatolian Fault Zone: Journal of the Geological Society, v. 180, https://doi.org/10.1144/jgs2023-020

Karabulut, H., Güvercin, S. E., Hollingsworth, J., Konca, A., Ö., 2023, Long silence on the East Anatolian Fault Zone (Southern Turkey) ends with devastating double earthquakes (6 February 2023) over a seismic gap: implications for the seismic potential in the Eastern Mediterranean region: Journal of the Geological Society, v. 180, https://doi.org/10.1144/jgs2023-021

Lin, A., Guo, J. Fu, B., 2004, Co-seismic mole track structures produced by the 2001 Ms 8.1 Central Kunlun earthquake, China: Journal of Structural Geology, v. 26 (8), p.1511-1519, https://doi.org/10.1016/j.jsg.2004.01.005

Lin, A., Nishikawa, M., 2011, Riedel shear structures in the co-seismic surface rupture zone produced by the 2001 Mw 7.8 Kunlun earthquake, northern Tibetan Plateau: Journal of Structural Geology, v. 33 (9) , p.1302-1311, https://doi.org/10.1016/j.jsg.2011.07.003

Liu, C., Lay, T., Wang, R, Taymaz, T., Xie, Z., Xiong, X., Irmak, T., S., Kahraman, M., Erman, C., 2023, Complex multi-fault rupture and triggering during the 2023 earthquake doublet in southeastern Türkiye: Nature Communications, v. 14, https://doi.org/10.1038/s41467-023-41404-5

Manzocchi, T., 2002, The connectivity of two-dimensional networks of spatially correlated fractures: Water Resources Research, v. 38 (9), https://doi.org/10.1029/2000WR000180

Meng, J., Kusky, T., Mooney, W., D., Bozkurt, E., Bodur, M., N., Wang, L., 2024, Surface deformations of the 6 February 2023 earthquake sequence, eastern Türkiye: Science, v. 383, p.298-305, 10.1126/science.adj3770

Naylor, M. A., Mandl, G., Sijpesteijn, C. H. K., 1986, Fault geometries in basement-induced wrench faulting under different initial stress states: Journal of Structural Geology, v. 8, p.737-752, https://doi.org/10.1016/0191-8141(86)90022-2

Özkan, A., Solak, H., I., Tiryakioğlu, I., Şentürk, M., D., Aktuğ, B., Gezgin, C., Poyraz, F., Duman, H., Masson, F., Uslular, G., Yiğit, C., O., Yavaşoğlu, H., H., 2023, Characterization of the co-seismic pattern and slip distribution of the February 06, 2023, Kahramanmaraş (Turkey)

earthquakes (Mw 7.7 and Mw 7.6) with a dense GNSS network: Tectonophysics, v. 866, https://doi.org/10.1016/j.tecto.2023.230041

Pennacchioni, G., Mancktelow, N. S, 2013, Initiation and growth of strike-slip faults within intact metagranitoid (Neves area, eastern Alps, Italy): GSA Bulletin, v.125, p. 1468-1483, https://doi.org/10.1130/B30832.1

Petersen, G., M., Büyükakpinar, P., Sanhueza, F., O., V., Metz, M., Cesca, S., Akbayram, K., Saul, J., Dahm, T., 2023, The 2023 Southeast Türkiye Seismic Sequence: Rupture of a Complex Fault Network: The Seismic Record, v. 3 (2), p. 134–143. https://doi.org/10.1785/0320230008

Piccardi, L., Vittori, E., Blumetti, A., M., Comerci, V., Di Manna, P., Guerrieri, L., Baglione, M., D'Intinosante, V., 2017, Mapping capable faulting hazard in a moderate-seismicity, high heat-flow environment: The Tuscia province (southern Tuscany-northern Latium, Italy): Quaternary International, v. 451, p. 11-36, https://doi.org/10.1016/j.quaint.2017.07.018

Quigley, M., Van Dissen, R., Litchfield, N., Villamor, P., Duffy, B., Barrell, D., Furlong, K., Stahl, T., Bilderback, E., Noble D., 2012, Surface rupture during the 2010 Mw7.1 Darfield (Canterbury) earthquake: Implications for fault rupture dynamics and seismic-hazard analysis: Geology, v. 40 (1), p. 55–58, https://doi.org/10.1130/G32528.1

Reitman, N., G., Briggs, R., W. Barnhart, W., D., Hatem, A., E., Thompson Jobe, J., A., DuRoss, C., B., Gold, R., C., Mejstrik, J., D., Collett, C., Koehler, R., D., Sinan Akçiz, S., 2023, Rapid Surface Rupture Mapping from Satellite Data: The 2023 Kahramanmaraş, Turkey (Türkiye), Earthquake Sequence: The Seismic Record, v.3 (4), p. 289–298, https://doi.org/10.1785/0320230029

Ren, J., Zhang, Z., Gai, H., Kang, W., 2021, Typical Riedel shear structures of the coseismic surface rupture zone produced by the 2021 Mw 7.3 Maduo earthquake, Qinghai, China, and the implications for seismic hazards in the block interior: Natural Hazards Research, v. 1(4), https://doi.org/10.1016/j.nhres.2021.10.001

Richard, P., Naylor, M.A., Koopman, A., 1995, Experimental models of strike-slip tectonics: Petroleum Geoscience, v. 1, p. 71–80, https://doi.org/10.1144/petgeo.1.1.71

Riedel, W, 1929, Zur Mechanik geologischer Brucherscheinungen: Zentralblatt fur Mineralogie, Geologie und Paleontologie p. 354-368

Sun, Q., Fan, T., Holdsworth, R. E., Gao, Z., Wu, J., Gao, S., Wang, M., Yuan, Y., 2023, The spatial characterization of stepovers along deeply-buried strike-slip faults and their influence on reservoir distribution in the central Tarim Basin, NW China: Journal of Structural Geology, v. 170, https://doi.org/10.1016/j.jsg.2023.104849

Swanson, M. T., 2006, Late Paleozoic strike-slip faults and related vein arrays of Cape Elizabeth, Maine: Journal of Structural Geology, v. 28 (3), p. 456-473, https://doi.org/10.1016/j.jsg.2005.12.009

Tchalenko, J. S., 1970, Similarities between shear zones of different magnitudes: Geological Society of America Bulletin, v. 81, p. 1625-1640, https://doi.org/10.1130/0016-7606(1970)81[1625:SBSZOD]2.0.CO;2

Tchalenko, J. S., and Ambraseys, N. N., 1970, Structural Analysis of the Dasht-e Bayaz (Iran) Earthquake Fractures: Geological Society of America Bulletin, v. 81 1, p. 41-60, https://doi.org/10.1130/0016-7606(1970)81[41:SAOTDB]2.0.CO;2

Toker, M., Yavuz, E., Utkucu, M., Uzunca, F., 2023, Multiple segmentation and seismogenic evolution of the 6th February 2023 (Mw 7.8 and 7.7) consecutive earthquake ruptures and aftershock deformation in the Maras triple junction region of SE-Anatolia, Turkey: Physics of the Earth and Planetary Interiors, v. 345, https://doi.org/10.1016/j.pepi.2023.107114

Ueta, K., Tani, K., Kato, T., 2000, Computerized X-ray tomography analysis of three-dimensional fault geometries in basement-induced wrench faulting: Engineering Geology, v. 56, p. 197-210, https://doi.org/10.1016/S0165-1250(00)80019-X

Wilkox, R., E., Harding, T., P., and Seely, D., R., 1973, Basic Wrench Tectonics: The American Association of Petroleum Geologists Bullettin, v. 57 (1), p. 74-96, https://doi.org/10.1306/819A424A-16C5-11D7-8645000102C1865D

Yang, X., Guanghui, W., Yongliang, L., Tingting, C., 2017, Analogue modeling of through-going process and development pattern of strike-slip fault zone: Petroleum exploration and development, v. 44 (3), p. 368-376, https://doi.org/10.1016/S1876-3804(17)30043-5

Yuan, Z., Li, T., Su, P., Sun, H., Ha, G., Guo, P., Chen, G., Thompson Jobe, J., 2022, Large surface-rupture gaps and low surface fault slip of the 2021 Mw7.4 Maduo earthquake along a low-activity strike-slip fault, Tibetan Plateau: Geophysical Research Letters, v. 49, https://doi.org/10.1029/2021GL096874

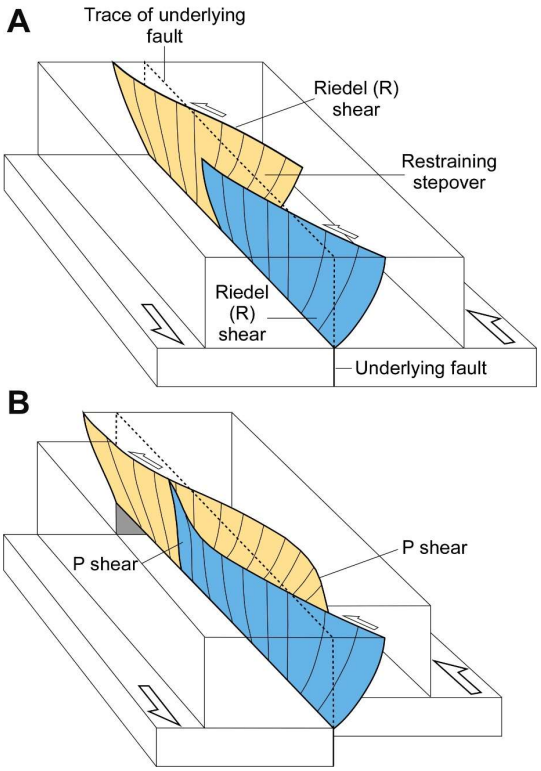

374

375 **Figure 1**

376

377

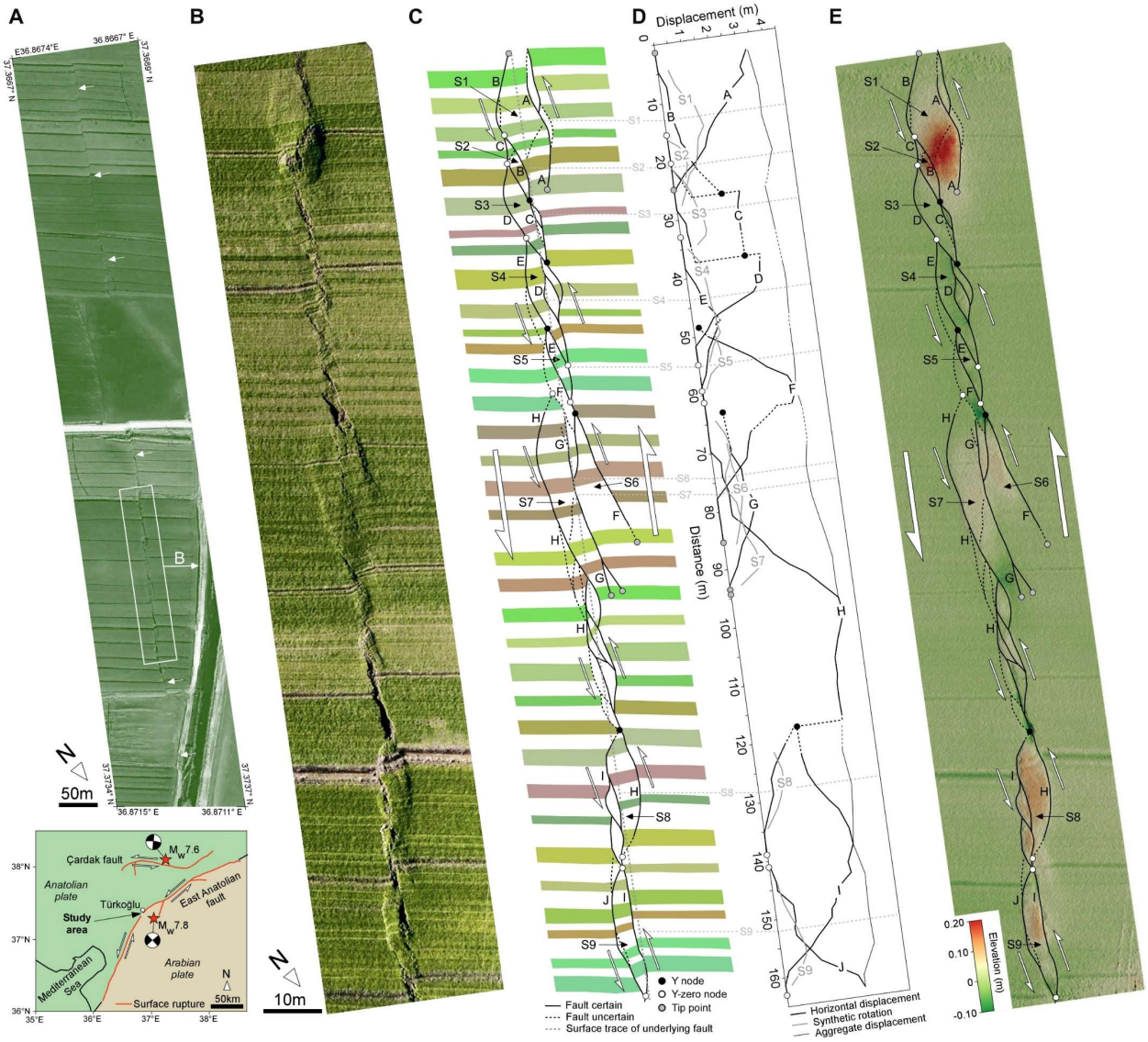
A
B
C
D
E
Displacement (m)
Distance (m)
Elevation (m)
50m
10m
N
Çardak fault
Anatolian plate
Türkoğlu
Study area
East Anatolian fault
Arabian plate
Mediterranean Sea
Surface rupture
50km
Fault certain
Fault uncertain
Surface trace of underlying fault
Y node
Y-zero node
Tip point
Horizontal displacement
Synthetic rotation
Aggregate displacement

Figure 2

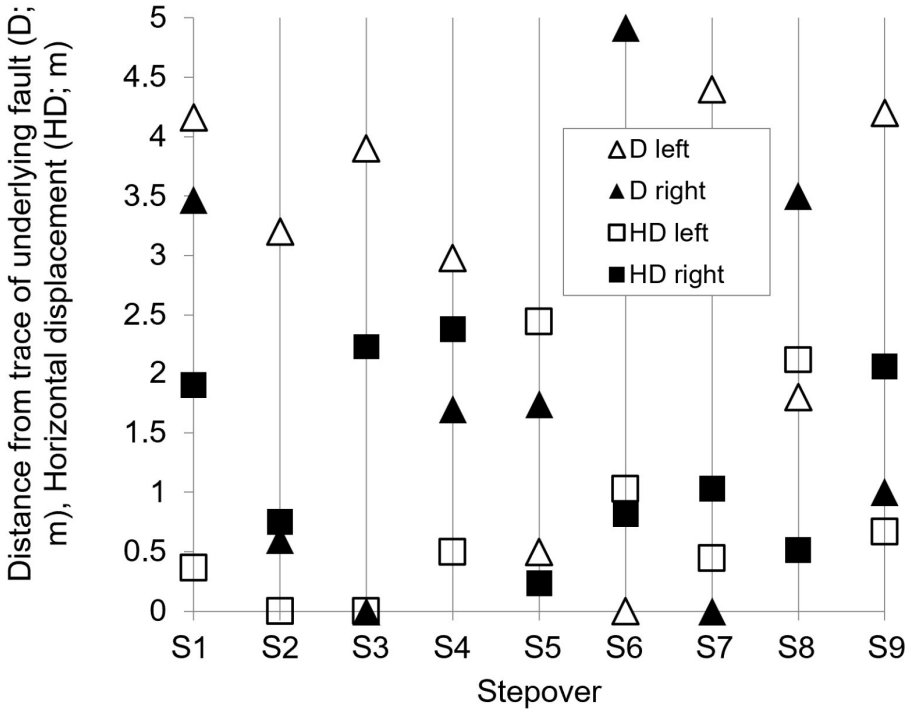

382

383 **Figure 3**

384

385

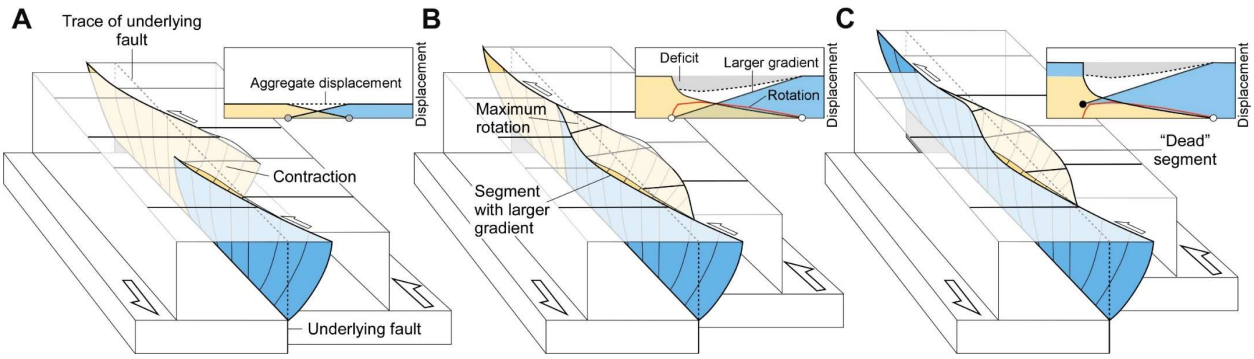

386

387 **Figure 4**